

FADEC: FPGA-based Acceleration of Video Depth Estimation by HW/SW Co-design

Nobuho Hashimoto*, Shinya Takamaeda-Yamazaki†
The University of Tokyo

*hashimoto-nobuho949@g.ecc.u-tokyo.ac.jp, †shinya@is.s.u-tokyo.ac.jp

Abstract—3D reconstruction from videos has become increasingly popular for various applications, including navigation for autonomous driving of robots and drones, augmented reality (AR), and 3D modeling. This task often combines traditional image/video processing algorithms and deep neural networks (DNNs). Although recent developments in deep learning have improved the accuracy of the task, the large number of calculations involved results in low computation speed and high power consumption. Although there are various domain-specific hardware accelerators for DNNs, it is not easy to accelerate the entire process of applications that alternate between traditional image/video processing algorithms and DNNs. Thus, FPGA-based end-to-end acceleration is required for such complicated applications in low-power embedded environments.

This paper proposes a novel FPGA-based accelerator for DeepVideoMVS, which is a DNN-based depth estimation method for 3D reconstruction. We employ HW/SW co-design to appropriately utilize heterogeneous components in modern SoC FPGAs, such as programmable logic (PL) and CPU, according to the inherent characteristics of the method. As some operations are unsuitable for hardware implementation, we determine the operations to be implemented in software through analyzing the number of times each operation is performed and its memory access pattern, and then considering comprehensive aspects: the ease of hardware implementation and degree of expected acceleration by hardware. The hardware and software implementations are executed in parallel on the PL and CPU to hide their execution latencies. The proposed accelerator was developed on a Xilinx ZCU104 board by using NNGen, an open-source high-level synthesis (HLS) tool. Experiments showed that the proposed accelerator operates 60.2 times faster than the software-only implementation on the same FPGA board with minimal accuracy degradation. Code available: <https://github.com/casys-utokyo/fadec/>

Index Terms—Depth estimation, DeepVideoMVS, HW/SW co-design, FPGA, Deep neural network

I. INTRODUCTION

Video processing has been studied for many years, including tasks ranging from classical video compression to object detection. These methods have been improved by the recent development of deep learning, achieving high degrees of accuracy and quality that surpass those of the classical methods. However, for 3D reconstruction from videos, there is room for further improvement in terms of both speed and accuracy. Highly accurate and dense 3D information has become particularly important because it is used in a wide range of applications, such as navigation for autonomous driving of robots and drones [1], augmented reality (AR) [2], [3], and 3D modeling [4]. However, obtaining such information usually requires expensive equipment or complex computation.

Active sensing, which often uses light detection and ranging (LiDAR) devices [5] or time-of-flight (ToF) cameras [6], has the disadvantages of requiring expensive devices and specific conditions to work well [7]. Passive sensing using monocular or stereo cameras can overcome these disadvantages, but the use of stereo cameras has the disadvantage of requiring large baselines and careful calibrations using multiple cameras [7]. Thus, 3D reconstruction from videos obtained using a regular monocular camera is becoming increasingly important.

For such 3D reconstruction, depth estimation is the fundamental task for estimating the distance between the camera and target object. DeepVideoMVS [8] is a DNN-based scene-independent depth estimation method that does not require per-scene training after pre-training. This method is a complex algorithm that combines traditional image/video processing algorithms and DNNs consisting of 96 convolutional neural networks (CNNs), including a recurrent neural network (RNN) called ConvLSTM [9]. Although there are various domain-specific hardware accelerators for DNNs, it is not easy to accelerate the entire process of applications that alternate between traditional image/video processing algorithms and DNNs. Thus, FPGA-based end-to-end acceleration is required for such complicated applications in low-power embedded environments.

In this study, we propose a novel FPGA-based accelerator for DeepVideoMVS. We employ HW/SW co-design to appropriately utilize heterogeneous components in modern SoC FPGAs, such as programmable logic (PL) and CPU, according to the inherent characteristics of the method. The implementations on the PL and CPU are designed to work parallelly and cooperatively. We developed this accelerator on the Xilinx ZCU104 board. We also demonstrated that it runs at high speed with minimal accuracy degradation. The main contributions of this study are summarized as follows.

- 1) We proposed an FPGA-based accelerator for the complex depth estimation method, DeepVideoMVS, that combines traditional image/video processing algorithms and DNNs. We employed HW/SW co-design to appropriately utilize heterogeneous components in modern SoC FPGAs, such as PL and CPU.
- 2) We designed custom circuits for the hardware-friendly processes, including large DNNs with practical sizes, on the PL using a high-level synthesis (HLS) tool.
- 3) We designed optimized programs for the software-

friendly processes on the CPU and combined the hardware and software implementations for parallel execution on the PL and CPU to hide their execution latencies.

- 4) We implemented the proposed accelerator on the Xilinx ZCU104 board. The computation speed was 60.2 times faster than that of the software-only implementation on the same FPGA board.

II. BACKGROUND

A. Depth Estimation

Stereo matching and triangulation are basic principles used for depth estimation. Stereo matching is used to estimate disparities, which are defined as the difference in position between each point in one image and its corresponding point in another image. Triangulation is then used to calculate the distance between the camera and each point. However, because it is not easy to find the corresponding points, it is common to estimate the disparities as follows. First, the matching cost is calculated, which is expressed as the similarity between the patches of the two images. Next, multiple candidate disparities are prepared and a 3D cost volume that stores the matching costs assuming each disparity are created. By optimizing the entire cost volume, the disparity for each pixel is estimated.

Traditionally, a method that sequentially performs structure from motion (SfM) and multi-view stereo (MVS) has been used to solve depth estimation tasks. SfM estimates the camera poses, which are represented as a 4×4 matrix for projection from camera coordinates to global coordinates and recovers low-density 3D information using the stereo matching principle. MVS then transforms this information into high-density 3D information. However, SfM outputs are susceptible to camera shaking, motion blurring, moving objects, and occlusion, and MVS outputs often contain several holes and noises [10], [11]. Thus, learning-based algorithms are also used; however, they often produce inaccurate outputs with little geometric consistency, although the outputs are plausible.

Hybrid methods combining traditional and learning-based methods have also been studied [10]–[12]. These methods achieve more accurate outputs using DNNs for SfM and MVS processes. Furthermore, they can maintain geometric consistency by devising optimization to obtain more accurate poses and adding geometric corrections using the poses to the inputs and intermediate outputs. However, because their computations are slow owing to DNNs that require a large number of calculations, some studies aim for a fast and lightweight system by changing the DNN structure and image resolution [8], [13].

The hybrid algorithms described thus far are designed to enable depth estimation in various scenes by training once with datasets. By contrast, some depth estimation methods learn static or dynamic 3D spatial representations of a particular scene using images or videos from multiple viewpoints [14]–[17]. Owing to the characteristics of these methods, they provide higher accuracy; however, they must be trained again for use in different scenes. Therefore, they are unsuitable for real-time applications in which various scenes are inputted.

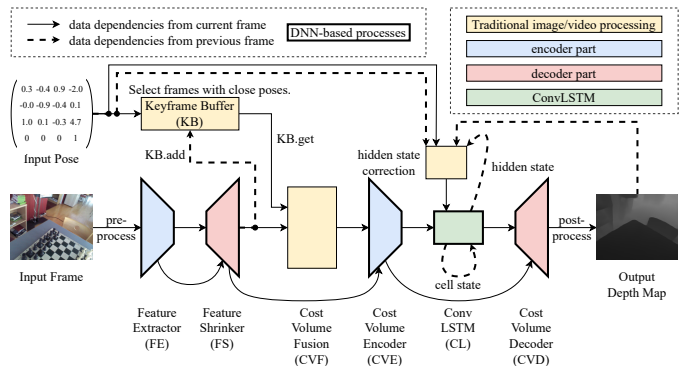


Fig. 1: Diagram of DeepVideoMVS. Although KB stores input images in the original study, KB stores the FS output features instead to reduce the number of calculations in this study. The arrows indicate data dependencies, and the bold dotted arrows show dependencies from each data obtained by processing one previous frame. The areas surrounded by a bold line indicate that the processes are mainly based on DNNs.

This study aims to accelerate such a complex depth estimation algorithm in low-power embedded environments. Thus, we selected DeepVideoMVS, which does not require pre-scene training and is expected to operate at near real-time speed.

B. DeepVideoMVS

Fig. 1 shows a diagram of DeepVideoMVS [8], which is used for depth estimation. This figure also shows the processes performed in this method and their data dependencies. This method uses DNNs and estimates depth maps through stereo matching with previous frames using the video and camera poses of each video frame. The key feature of the DNN model is that it can be applied to a wide range of situations with high accuracy once trained using training datasets due to its complex processing mechanism. Here, we outline the processes of the method necessary for this study (see [8] for further details).

1) *Processes Based on DNNs*: In Fig. 1, the feature extractor (FE) uses MnasNet [18] and the feature shrinker (FS) uses a feature pyramid network (FPN) [19]. These networks extract image features and increase the receptive field. The cost volume encoder (CVE) and cost volume decoder (CVD) are similar to an encoder-decoder network with skipping connections, such as U-Net [20]. These are used to normalize the raw cost volume in the spatial direction. Moreover, the incorporation of ConvLSTM (CL) in the middle enables the use of time-series information specific to videos. CL uses the sigmoid and ELU [21], which are nonlinear activation functions, and also uses layer normalization [22] instead of batch normalization (BN).

2) *Processes Based on Traditional Image/Video Processing Algorithms*: In Fig. 1, the keyframe buffer (KB), cost volume fusion (CVF), and hidden state correction are mainly related to traditional image/video processing algorithms. KB stores the FS output, which is an image feature, along with the camera pose. The feature is retrieved and reused when a frame with a

similar pose appears as input. This process can help improve the accuracy because information on previous similar scenes is available. CVF first converts past features into those observed from the current viewpoint by grid sampling using past and current poses. The converted features are used to obtain the cost volume from the current feature. Similarly, grid sampling is also performed to apply viewpoint changes to the previous hidden state. Grid sampling is formulated as follows:

$$\begin{aligned} (i, j) &= (\lfloor \mathbf{g}_{s,t,0} \rfloor, \lfloor \mathbf{g}_{s,t,1} \rfloor) \\ (k, l) &= (\mathbf{g}_{s,t,0} - \lfloor \mathbf{g}_{s,t,0} \rfloor, \mathbf{g}_{s,t,1} - \lfloor \mathbf{g}_{s,t,1} \rfloor) \\ \mathbf{y}_{s,t} &= (1-k) \cdot (1-l) \cdot \mathbf{x}_{i,j} + (1-k) \cdot l \cdot \mathbf{x}_{i,j+1} \\ &\quad + k \cdot (1-l) \cdot \mathbf{x}_{i+1,j} + k \cdot l \cdot \mathbf{x}_{i+1,j+1}, \end{aligned}$$

where \mathbf{g} denotes a grid, \mathbf{x} and \mathbf{y} denote the input and output, respectively, and (i, j) and (k, l) denote the integer and fractional parts of $\mathbf{g}_{s,t}$, respectively.

3) *Dataflow*: In Fig. 1, the input pose, CL cell state, CL hidden state, and final output depth map must be passed on to the processing of the next frame. In KB, the input pose alone is sufficient to obtain the input for CVF; however, the FS output must also be stored before the next input image is processed. In this manner, we consider the timing of when each process needs to be completed. A deep understanding of the dataflow is essential for accelerating the entire process, particularly when inputs are given consecutively.

III. FADEC

This study proposes FPGA-based end-to-end acceleration for DeepVideoMVS in low-power embedded environments. Modern SoC FPGAs contain PL and CPU; the PL can be easily manipulated using a framework such as PYNQ, the CPU core is fast, and they share memory. Thus, HW/SW co-design has become common in recent years. To accelerate the entire process, it is important to assign each process to the PL and CPU at an appropriate time.

The overall procedure is as follows: 1) *HW/SW Co-design*: We examine whether each operation should be implemented in hardware or software, taking advantage of the characteristics of hardware and software. 2) *HW Design*: We design custom circuits for the hardware-friendly processes on the PL using an HLS tool. 3) *SW Design*: We design optimized programs for the software-friendly processes on the CPU. 4) *HW/SW Scheduling*: We combine the hardware and software implementations such that they are executed in parallel on the PL and CPU to hide their execution latencies.

A. HW/SW Co-design

We first analyze the number of times each operation is performed and its memory access pattern, and then consider comprehensive aspects: the ease of hardware implementation and degree of expected acceleration by hardware. Finally, we examine whether each operation should be implemented in hardware or software by taking advantage of the characteristics of hardware and software.

TABLE I: Number of operations performed in each major process of DeepVideoMVS. The numbers to the right of *conv* represent (kernel size, stride).

Operation	Process	FE	FS	CVF	CVE	CL	CVD
Conv (1, 1)		33	5	0	0	0	0
Conv (3, 1)		6	4	0	9	1	14
Conv (3, 2)		2	0	0	3	0	0
Conv (5, 1)		7	0	0	3	0	5
Conv (5, 2)		3	0	0	1	0	0
Activation (ReLU)		34	0	0	16	0	14
Activation (sigmoid)		0	0	0	0	3	5
Activation (ELU)		0	0	0	0	2	0
Addition		10	4	128	0	1	0
Multiplication		0	0	64	0	3	0
Concatenation		0	0	0	4	1	5
Slice		0	0	0	0	4	0
Layer Normalization		0	0	0	0	2	9
Upsampling (nearest)		0	4	0	0	0	0
Upsampling (bilinear)		0	0	0	0	0	9
Grid Sampling		0	0	128	0	0	0

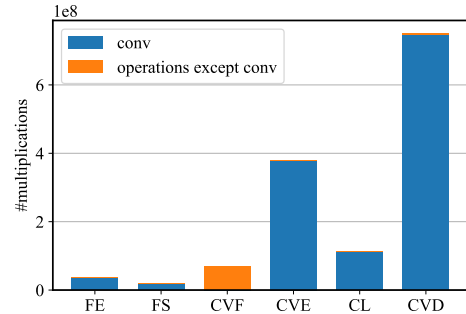


Fig. 2: Comparison of the number of multiplications performed in each major process of DeepVideoMVS.

1) *Number of Multiplications*: Table I outlines the operations performed in each major process of DeepVideoMVS. These operations mainly consist of addition and multiplication operations. Thus, Fig. 2 summarizes the number of multiplications, which are more of a bottleneck than an addition, considering each tensor size. CVE and CVD for cost volume processing together make up 82.4% of the total multiplications. Other processes, such as storing data in KB and correcting hidden states, are not included because they require few calculations. Thus, CVE and CVD should be prioritized for hardware acceleration to eliminate bottlenecks. In these processes, the multiplications required for the *conv* calculation account for more than 99% of the total multiplications. Thus, it is essential to accelerate *conv* in hardware, which would also accelerate the other processes. Eventually, CVF, which does not involve *conv*, becomes a bottleneck.

2) *Memory Access Pattern*: Next, we examine the memory access patterns of the operators in Table I.

Conv and upsampling: These operators access memory in the manner of a sliding window. This access pattern has high data reuse, and *conv* is particularly suitable for hardware implementation because of the bottleneck in its operations.

Activation: As this is usually folded into *conv*, it is unnecessary to consider its memory access.

Addition and multiplication: As these are element-wise operators, their bottlenecks are in memory bandwidth. Thus, there is no significant difference in the performance between the hardware and software executions.

Concatenation and slice: As these memory access patterns are almost sequential, their bottlenecks are in memory bandwidth. Thus, there is no significant difference in the performance between the hardware and software executions.

Layer normalization: All values are scanned to obtain the mean and variance of each layer; this scanning is then repeated for normalization. Thus, each element is accessed twice, which makes this operator more intensive in memory bandwidth than previous ones. There is also no significant difference in the performance between the hardware and software executions.

Grid sampling: This operator performs bilinear interpolation to obtain the value at the position represented by the coordinates specified for each element. Thus, the access pattern varies significantly, depending on the specified coordinates. As this operator requires irregular access, accelerating it by hardware is difficult.

3) *HW/SW Partitioning*: We determine whether each process should be implemented in hardware or software. Among the operations in Table I, we examine the hardware implementation of the following six operations: *conv*, *activation (sigmoid)*, *activation (ELU)*, *layer normalization*, *upsampling (bilinear)*, and *grid sampling*. Hardware acceleration methods for *conv* through quantization and parallelization are well known. The nonlinear activation functions (*sigmoid* and *ELU*) can be implemented in a lightweight manner by approximating the exponential functions using LUTs. By contrast, *layer normalization* is difficult to accelerate using hardware while maintaining high precision because it requires square root and division operations to normalize each layer. It is also unlikely that *upsampling (bilinear)* can be significantly accelerated by hardware because the memory access pattern is slightly irregular and floating-point arithmetic operations are suitable for high precision. Thus, it is considered acceptable to implement it in software by using floating-point arithmetic to ensure precision. Finally, because *grid sampling* requires bilinear interpolation and its memory access pattern is irregular, the software implementation is preferable for this operation.

The HW/SW partitioning of the processes in Fig. 2 is summarized as follows:

FE, FS, CVE, and CVD: As these are mainly composed of *conv*, these should be implemented in hardware except for *upsampling (bilinear)*.

CL: This process should also be implemented in hardware except for *layer normalization*.

CVF: In this process, 64 *grid sampling* operations are performed twice, and the results are added together to obtain 64 tensors with the same shape as the current feature. These tensors are then multiplied by the current feature and summed in the channel direction to obtain the cost volume. As *grid sampling* is executed in software, it is reasonable to send the current feature from hardware to software, perform the rest of

the processes in software, and pass the output to hardware. Compared to the case where the rest of the processes is performed in hardware, the communication between hardware and software can be reduced to 2/64. Furthermore, because the number of multiplications in CVF accounts for only 5.0% of the total, its execution latency can be hidden by parallelizing it with hardware execution as much as possible, even if its computation is slightly slow.

Operations not included in Fig. 2: These are implemented in software for simplicity because a few calculations are required.

B. HW Design

Here, we describe the implementation of the hardware-friendly processes on PL using an HLS tool. First, the algorithms and parameters should be changed to make them suitable for hardware through BN folding, quantization, and approximation. The design is then implemented in hardware and parallelized.

1) *BN Folding*: Recent DNN models, including DeepVideoMVS, often use a BN layer after a convolution layer. The BN plays an important role in training to increase accuracy by normalizing activation values; however, in inference, it simply affine transforms them with fixed trained parameters. Therefore, in inference, the BN can be folded with the convolution to reduce the number of calculations [23].

2) *Quantization*: Here, we quantize the trained parameters using the PTQ (Post-Training Quantization) method, without any other modifications. Quantization is performed per tensor and not per channel.

We explain the PTQ performed in this study using *conv* as an example. The *conv* calculation before the PTQ is shown as

$$\mathbf{y}_{i,j} = \left(\sum_{s,t} (\mathbf{W}_{s,t} \cdot \mathbf{x}_{i+s,j+t}) + b \right) \cdot s,$$

where \mathbf{W} , b , and s denote the weight, bias, and scale, respectively, and \mathbf{x} and \mathbf{y} denote the activation values of the input and output, respectively. The calculation after the PTQ is as follows:

$$\hat{m}_1 = \sum_{s,t} (\hat{\mathbf{W}}_{s,t} \cdot \hat{\mathbf{x}}_{i+s,j+t}) + \hat{b}$$

$$\hat{m}_2 = \hat{m}_1 \cdot \hat{s}$$

$$\hat{\mathbf{y}}_{i,j} = \text{clip}(\text{rshift}(\hat{m}_2, r)),$$

where m_1 and m_2 denote the intermediate outputs. The variables with $\hat{\cdot}$ indicate the values after the PTQ, and r expresses a right shift amount of \hat{m}_2 to adjust the numerical ranges of \hat{m}_2 and $\hat{\mathbf{y}}_{i,j}$ values. Function *rshift* expresses the r -bit right shift and rounding of \hat{m}_2 . Function *clip* clips the input out of range such that the input falls within the range of the quantization bit of $\hat{\mathbf{y}}$.

First, we determine the quantization bits for the weights, biases, scales, and activation values. These values should be selected as the smallest possible values that satisfy the target accuracy by attempting quantization and inference. Next, we quantize each value and determine the quantization parameters. The quantization parameters indicate the quantized values

of the weights, biases, and scales, as well as the multipliers used to quantize the weights, biases, scales, and activation values. The weights, biases, and scales are multiplied by the largest power of two such that all values fall within the range of each quantization bit. To quantize the activation values, we first prepare several images from the dataset or random images with the same mean and variance as the dataset images. We then collect the activation values for each layer by inferring them. Finally, the collected values are multiplied by the largest power of two such that more than $\alpha\%$ values fall within the range of each quantization bit, where α is an appropriate clipping rate. Setting all multipliers to the powers of two simplifies several processes. For example, when two activation values are added or concatenated, their numerical ranges must be the same. In this PTQ setting, at most one left shift (*lshift*) is sufficient to adjust these ranges. Consequently, this setting simplifies the implementation, reduces errors, and eliminates division operations. By contrast, the bit width cannot be used as effectively if constant multipliers other than those of powers of two are allowed.

This quantization method allows operations, including *conv*, *addition*, and *multiplication*, to be calculated within an integer range, which is expected to save hardware resources and accelerate these operations.

3) *LUT-based Approximation*: The *sigmoid* and *ELU* activation functions used in this study include exponential operations as follows:

$$\text{sigmoid}(x) = \frac{1}{1 + e^{-x}}$$

$$\text{elu}(x) = \begin{cases} x & (x \geq 0) \\ e^x - 1 & (x < 0) \end{cases}$$

If these are straightforwardly implemented in hardware, the execution time will be large. Thus, we approximate them using LUTs. The range of their input x (e.g., $-t \leq x \leq t$) is evenly divided by the number of table entries and the output values for each entry are stored in the table. However, if an input exceeding the specified input range is provided, the LUT returns the value at the closest end of the table. Here, the *sigmoid* table size can be reduced by half by using symmetry.

4) *Overall Hardware Architecture*: Next, we describe the overall hardware accelerator architecture of the processes to be implemented on the PL as shown in Fig. 3. A hardwired finite state machine (FSM) in this circuit (not presented in Fig. 3) automatically controls the operations. Dedicated arithmetic pipelines consisting of operators are prepared for each stage according to the stage type. In other words, the circuits for an arithmetic pipeline or combination of operations in a stage can be reused if another stage performs the same pipeline and combination as those in this stage. *Extern*, *shift*, and *clip*, which are not included in Table I, are used to quantize the activation values. Additionally, because element-wise operators, such as *addition*, *multiplication*, and *shift*, can continuously process a single value, the sequence of these operators can be folded into one.

5) *Data-level Parallelization*: We apply data-level parallelization to the architecture described thus far for further acceleration. When parallelizing operations, it is important to

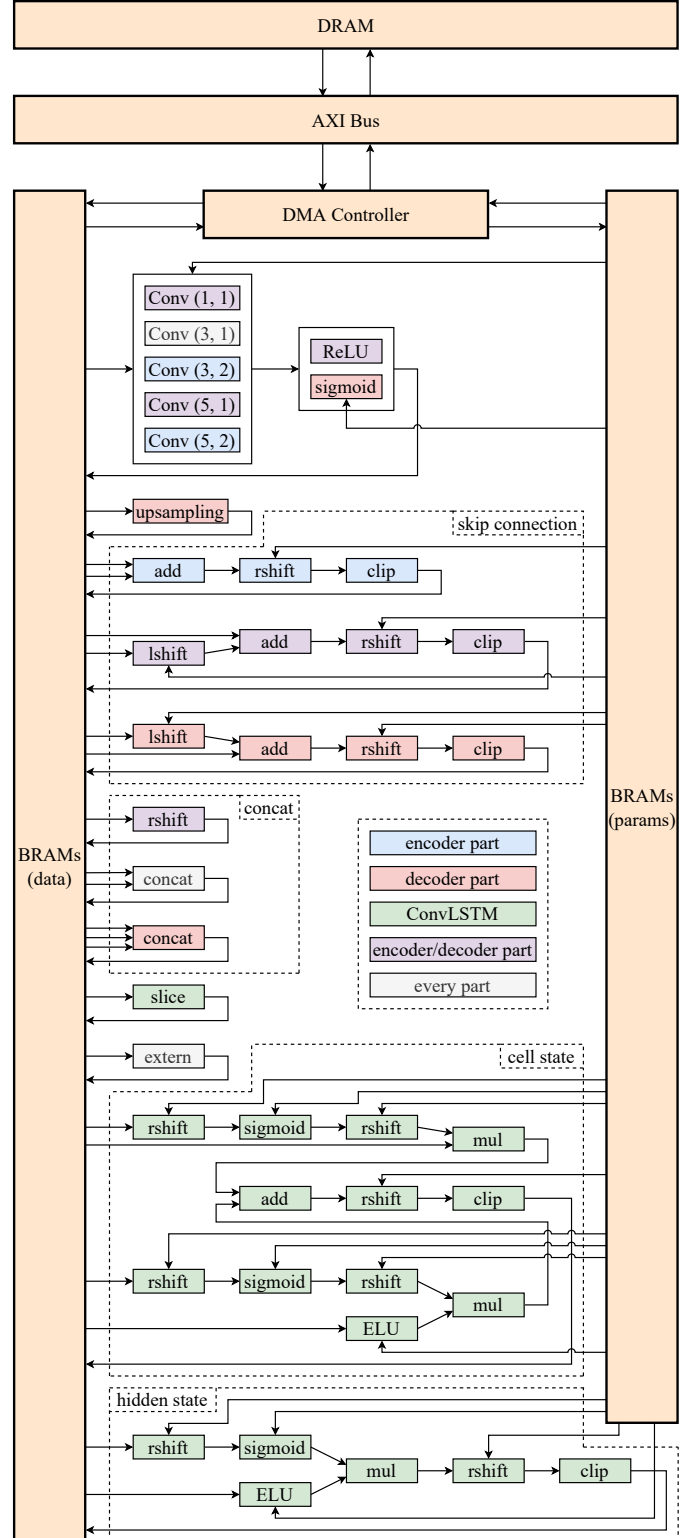


Fig. 3: Overall hardware accelerator architecture including dedicated arithmetic pipelines. *Extern* shows an operation to communicate with software (see section III-D1 for further details).

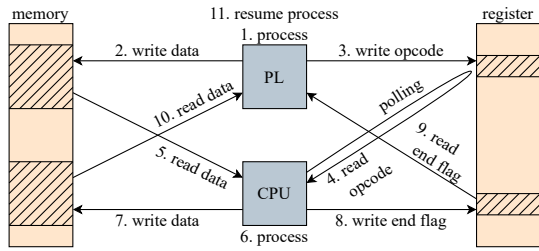


Fig. 4: Illustration of the interrupt handling mechanism between the PL and CPU. This operation corresponds to *extern* in Fig. 3.

consider the trade-off between execution speed and practical constraints, such as hardware resources and power consumption. In this study, parallelization was performed such that hardware resource constraints were satisfied. As *conv* has the largest number of multiplications, it should be preferentially parallelized. It can be parallelized for each input and output channel. Theoretically, the speed can be increased by a factor of the value obtained by multiplying the degrees of parallelism. Other operators, except for *concatenation*, *slice*, and *extern*, can also be parallelized for each channel. Theoretically, the speed can be increased by a factor of the degree of parallelism.

C. SW Design

We propose a design for the software-friendly processes, which can receive data from the PL and execute the process on the CPU when the PL specifies the process. To execute these processes at high speed, they should be implemented in an appropriate language using the same procedures and content as those for normal software development.

Although there are various acceleration methods for software processing, the methods used in this study are as follows:

- Optimize memory access patterns to increase the cache hit rate.
- Embed pre-determined variables.
- Perform quantization.
- Perform multithreaded parallelization.

Various optimization methods can be considered depending on the software and language specifications; however, in general, the above optimization methods can be used to speed up software processing.

D. HW/SW Scheduling

Finally, the hardware and software implementations are combined, and the PL and CPU processes are parallelized for acceleration. At this time, we hide the execution latencies by taking advantage of the fact that frames are given consecutively, and accelerate the time-consuming processes that are the bottlenecks in the pipeline.

1) *HW/SW Communication*: To notify the end of each process and exchange data, communication between hardware and software is necessary. This operation corresponds to *extern* in Fig. 3, which is achieved using a contiguous memory allocator (CMA) and interrupt handling mechanism. For communication between hardware and software, a mechanism to

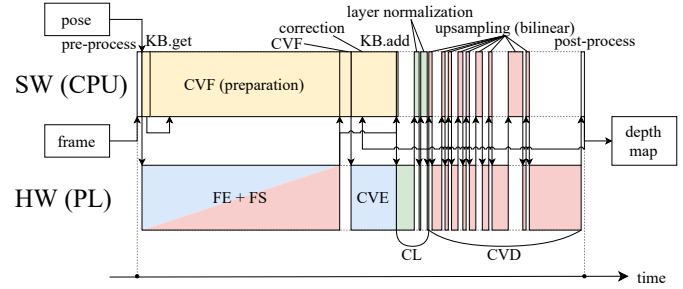


Fig. 5: Pipeline chart of the proposed accelerator. Arrows indicate data dependencies. The length of each process roughly corresponds to the actual execution latencies.

share memory space is required. However, hardware can only handle physical memory space, whereas software can handle virtual memory space. Thus, we use a contiguous physical memory area allocated using CMA. As data are exchanged within the memory area during execution, the allocated area should be sufficiently large to write the data shared by the PL and CPU. We also use the interrupt handling mechanism shown in Fig. 4 for the communication. Specifically, when the PL process finishes, the data are written to the memory, and an opcode representing the next CPU process is written to a specific register. When the CPU detects this by polling, it reads the data from the memory and executes the specified process. When the process is completed, the output is written to the memory and an end flag is set in a specific register. The PL then reads this flag and resumes the next process.

2) *Task-level Parallelization*: Fig. 5 shows a fully optimized pipeline chart. Before optimization, it is necessary to profile the execution latencies of each process in hardware and software. It is also important to consider the best place for each process to increase parallelism and hide execution latencies as much as possible. It may be necessary to devise methods to further accelerate certain processes.

For example, in this study, CVF is the most time-consuming software process, and the key to the entire acceleration is determining how to hide this latency. A detailed analysis of the dataflow reveals that only a small part of the process requires the FS output, and the other part (CVF (preparation)), including *grid sampling*, can be performed in parallel with the FE and FS execution in hardware. Thus, we can hide 93% of the total latency required for CVF. In addition, hidden state correction can also be performed in parallel with CVE execution to hide the latency. However, it is necessary to ensure that the correction process is completed at the beginning of CL, which requires the corrected hidden state. Thus, software is interrupted at the time, and the hardware process is resumed immediately after the correction process finishes.

IV. EVALUATION

In this section, we describe the implementation and performance evaluation of the proposed accelerator. The size of the input and output images is 96×64 , and a model pre-trained with TUM RGB-D [24], published by the authors of

TABLE II: Comparison of the execution time per frame between the processing of the proposed accelerator on the PL and CPU and that of the C++ implementation on the CPU-only.

Platform	median [s]	std [s]	frequency [MHz]
CPU-only	16.744	0.049	N/A
CPU-only (w/ PTQ)	13.248	0.035	N/A
PL + CPU (ours)	0.278	0.118	187.512

DeepVideoMVS, is used for inference. We use Python for the implementation and generate Verilog HDL codes using an open-source HLS tool called NNgen [25], [26] v1.3.3. We then generate a bitstream for the ZCU104 board with Zynq UltraScale+ MPSoC XCZU7EV-2FFVC1156 from Xilinx using Vivado 2021.2. Finally, we execute the proposed accelerator on the FPGA using PYNQ v2.6 for the ZCU104 board. PYNQ provides a Jupyter-based framework with Python APIs. Thus, the software processes that must be accelerated are written and compiled using Cython v0.29 to be executed in Python.

In the implementation, we set the parameters as follows. The quantization bits for the weights, biases, scales, and activation values are 8, 32, 8, and 16, respectively. To quantize the activation values, we set the clipping rate α to 95%. In LUT-based approximation, we set the number of entries to 256 and the input range t to 8.0. The degree of parallelism for *conv* was set to 2 in the input channel direction, 2 only when the kernel size was 5, and 4 in the other cases in the output channel direction. For other parallelizable operators, the degree was set to 4 in the channel direction. For the software processes, the degree was set to 2 because the Xilinx ZCU104 board has two cores.

We used 7-Scenes dataset [27] to evaluate the proposed accelerator using the following eight scenes: chess/seq-01, chess/seq-02, fire/seq-01, fire/seq-02, office/seq-01, office/seq-03, redkitchen/seq-01, and redkitchen/seq-07. As the error is calculated using the mean squared error (MSE) between the output and ground truth, a lower error value indicates a better output.

A. Execution Time

We compared the execution time between the processing of the proposed accelerator on the PL and CPU and that of the C++ implementation on the CPU-only using the Xilinx ZCU104 board. The C++ implementation was compiled using g++ 7.3.0 with the -O3 option on the board. The clock frequency of the proposed accelerator was 187.512 MHz, which is the frequency at which all timing constraints are met in Vivado. Table II shows the median and standard deviation of the time to finish processing a single image in the evaluation datasets. When the C++ implementation was run on the CPU-only, PTQ led to a slight reduction in execution time but not to a significant extent. The proposed accelerator drastically reduced the time, completing the tasks 60.2 times faster than the CPU-only execution.

We also considered the overhead required to perform *extern*, which is used to communicate between hardware and software. Overhead is defined as the difference between the waiting

TABLE III: Hardware resource utilization of the proposed accelerator on the Xilinx ZCU104 board.

Name	#Utilization	Available	Utilization [%]
Slice	28256	28800	98.1
LUT	176377	230400	76.6
FF	143072	460800	31.0
DSP	128	1728	7.41
BRAM	309	312	99.0

time in hardware and processing time in software, assuming that software processing can start immediately after being interrupted by hardware. The overhead includes the time required for software to read/write data and other control times. The median value of the measured overhead is 4.7 ms, which is 1.69% of the total execution time. Thus, the advantage of coordinating hardware and software outweighs the overhead.

B. Hardware Resources

Table III shows the hardware resource utilization of the proposed accelerator on the Xilinx ZCU104 board. The slices and block RAMs (BRAMs) are almost fully used, indicating that we can take full advantage of the hardware resources.

C. Accuracy

We evaluated the degree of accuracy loss due to PTQ and LUT-based approximation. First, a qualitative evaluation was performed using Figs. 6 and 7. The outputs of the proposed accelerator did not exhibit sufficient degradation in terms of accuracy to be visually distinguishable from the outputs of the C++ implementation. Next, we performed a quantitative evaluation using Fig. 8. Although the accuracy was slightly degraded compared with the C++ implementation for all scenes, the accuracy degradation remained below 10% in most cases. The accuracy of C++ with PTQ was lower than that of the proposed accelerator, which can be attributed to the fact that the proposed accelerator performs rounding after right shifts, whereas C++ with PTQ does not.

V. RELATED WORK

A. FPGA-based DNN Accelerator

In recent years, DNNs have been further improved in terms of accuracy at the expense of increased complexity. By contrast, on small edge or embedded devices, it is necessary to perform inference on such high-accuracy DNNs at high speed and low power consumption. Several studies have been conducted on DNN acceleration using FPGAs because FPGAs have attracted particular attention for such devices. ICAN [28] efficiently implements CNNs on an FPGA by devising a 3D data tiling. In addition, [29] devises memory allocation to read input and weight values in parallel, and reduces the number of calculations and hardware resource usage using XNOR-Net [30], a binary neural network. DNNBuilder [31] and DNNExplorer [32] design FPGA-based DNN accelerators automatically. Automatic design requires improving the efficiency of memory access and seeking a parallelization scheme by considering the amount of available hardware resources and

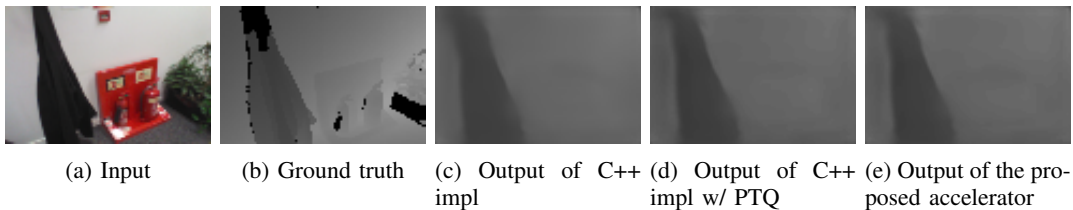


Fig. 6: Results of processing the frame number 000139 in the fire-seq-01 scene. The MSEs between the outputs and ground truth are (c) 0.091, (d) 0.073, (e) 0.089, and (f) 0.084, respectively.

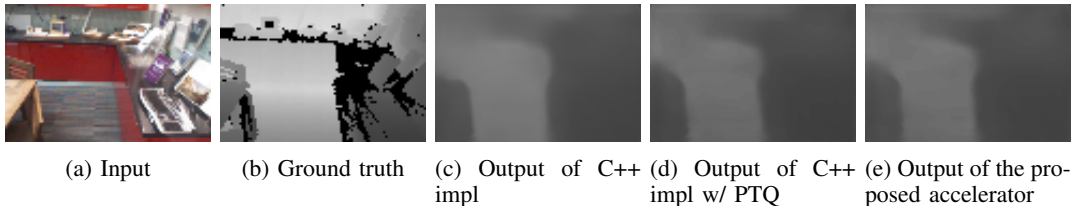


Fig. 7: Results of processing the frame number 000268 in the redkitchen-seq-07 scene. The MSEs between the outputs and ground truth are (c) 0.808, (d) 0.880, (e) 1.099, and (f) 1.050, respectively.

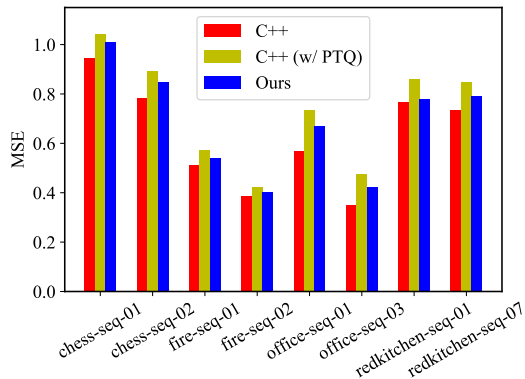


Fig. 8: Scene-by-scene difference between MSE obtained from the proposed accelerator and MSE obtained from the C++ implementation.

the complexity and characteristics of the DNN. These methods use DNNs with a maximum of 38 layers for evaluation, and few studies have been conducted on implementing more modern, larger DNNs on FPGAs.

B. HW/SW Co-design

HW/SW co-design has become increasingly popular for achieving lightweight and high-speed implementation. Several methods have been proposed to accelerate image/video processing, such as the visual odometry (VO) algorithm [33], histograms of oriented gradients (HOG) [34], and anisotropic diffusion filter (ADF) [35], using FPGAs. Although these methods are based on classical filtering methods, methods to accelerate the decision forest [36] and EfficientNet [37], which are machine learning techniques, have also been proposed. However, these methods aim to accelerate stand-alone algorithms, and few studies have been conducted on acceleration methods for large-scale, practical applications, such as

depth estimation that combines video processing and machine learning.

VI. CONCLUSION

This paper proposed a novel FPGA-based accelerator for DeepVideoMVS, which is a DNN-based depth estimation method for 3D reconstruction. DeepVideoMVS combines traditional image/video processing algorithms and DNNs, making it difficult to optimize the entire process. Thus, we employed HW/SW co-design to appropriately utilize heterogeneous components in modern SoC FPGAs, such as PL and CPU, according to the inherent characteristics of the method. As some operations are unsuitable for hardware implementation, we determined the operations to be implemented in software through analyzing the number of times each operation is performed and its memory access pattern, and then considering comprehensive aspects: the ease of hardware implementation and degree of expected acceleration by hardware. The hardware and software implementations were executed in parallel on the PL and CPU to hide their execution latencies. The proposed accelerator was developed on a Xilinx ZCU104 board. Experiments showed that the proposed accelerator operates 60.2 times faster than the software-only implementation on the same FPGA board with minimal accuracy degradation.

However, there is room for further reduction in hardware resource usage and improvement in terms of speed and accuracy. For example, because several new methods have been proposed for quantization and hardware implementation of convolution layers, smaller, faster, and more accurate implementations can be achieved by applying these techniques to the proposed accelerator.

ACKNOWLEDGMENT

This work is supported in part by JSPS KAKENHI 19H04075 and 18H05288, JST CREST JPMJCR21D2, and the collaboration research with KONICA MINOLTA.

REFERENCES

- [1] J. Delaune, R. Brockers, D. S. Bayard, H. Dor, R. Hewitt, J. Sawoniewicz, G. Kubiak, T. Tzanetos, L. Matthies, and J. Balaram, "Extended navigation capabilities for a future mars science helicopter concept," in *IEEE Aerospace Conference (AeroConf)*, 2020, pp. 1–10.
- [2] X. Luo, J. Huang, R. Szeliski, K. Matzen, and J. Kopf, "Consistent video depth estimation," *ACM Transactions on Graphics (TOG)*, vol. 39, no. 4, pp. 1–13, 2020.
- [3] J. Valentin, A. Kowdle, J. T. Barron, N. Wadhwa, M. Dzitsiuk, M. Schoenberg, V. Verma, A. Csaszar, E. Turner, I. Dryanovski, J. Afonso, J. Pascoal, K. Tsotsos, M. Leung, M. Schmidt, O. Guleryuz, S. Khamis, V. Tankovich, S. Fanello, S. Izadi, and C. Rhemann, "Depth from motion for smartphone AR," *ACM Transactions on Graphics (TOG)*, vol. 37, no. 6, pp. 1–19, 2018.
- [4] M. Yang, Y. Wen, W. Chen, Y. Chen, and K. Jia, "Deep optimized priors for 3D shape modeling and reconstruction," in *IEEE Conference on Computer Vision and Pattern Recognition (CVPR)*, 2021, pp. 3269–3278.
- [5] T. Raj, F. Hashim, A. Huddin, M. F. Ibrahim, and A. Hussain, "A survey on LiDAR scanning mechanisms," *Electronics*, vol. 9, 2020.
- [6] M. Hansard, S. Lee, O. Choi, and R. P. Horaud, *Time of Flight Cameras: Principles, Methods, and Applications*. Springer Science + Business Media, 2012.
- [7] F. Ma and S. Karaman, "Sparse-to-dense: Depth prediction from sparse depth samples and a single image," in *IEEE International Conference on Robotics and Automation (ICRA)*, 2018, pp. 4796–4803.
- [8] A. Duzceker, S. Galliani, C. Vogel, P. Speciale, M. Dusmanu, and M. Pollefeys, "DeepVideoMVS: Multi-view stereo on video with recurrent spatio-temporal fusion," in *IEEE Conference on Computer Vision and Pattern Recognition (CVPR)*, 2021, pp. 15 324–15 333.
- [9] X. Shi, Z. Chen, H. Wang, D. Yeung, W. Wong, and W. Woo, "Convolutional LSTM network: A machine learning approach for precipitation nowcasting," in *Advances in Neural Information Processing Systems*, vol. 28, 2015.
- [10] Z. Teed and J. Deng, "DeepV2D: Video to depth with differentiable structure from motion," in *International Conference on Learning Representations (ICLR)*, 2020.
- [11] J. Kopf, X. Rong, and J. Huang, "Robust consistent video depth estimation," in *IEEE Conference on Computer Vision and Pattern Recognition (CVPR)*, 2021, pp. 1611–1621.
- [12] J. S. Yoon, K. Kim, O. Gallo, H. S. Park, and J. Kautz, "Novel view synthesis of dynamic scenes with globally coherent depths from a monocular camera," in *IEEE Conference on Computer Vision and Pattern Recognition (CVPR)*, 2020.
- [13] V. Tankovich, C. Hane, Y. Zhang, A. Kowdle, S. Fanello, and S. Bouaziz, "HITNet: Hierarchical iterative tile refinement network for real-time stereo matching," in *IEEE Conference on Computer Vision and Pattern Recognition (CVPR)*, 2021, pp. 14 362–14 372.
- [14] B. Mildenhall, P. P. Srinivasan, M. Tancik, J. T. Barron, R. Ramamoorthi, and R. Ng, "NeRF: Representing scenes as neural radiance fields for view synthesis," in *European Conference on Computer Vision (ECCV)*, 2020, pp. 405–421.
- [15] Z. Li, S. Niklaus, N. Snavely, and O. Wang, "Neural scene flow fields for space-time view synthesis of dynamic scenes," in *IEEE Conference on Computer Vision and Pattern Recognition (CVPR)*, 2021, pp. 6498–6508.
- [16] A. Bansal, M. Vo, Y. Sheikh, D. Ramanan, and S. Narasimhan, "4D visualization of dynamic events from unconstrained multi-view videos," in *IEEE Conference on Computer Vision and Pattern Recognition (CVPR)*, 2020.
- [17] B. Yang, Y. Zhang, Y. Li, Z. Cui, S. Fanello, H. Bao, and G. Zhang, "Neural rendering in a room: Amodal 3D understanding and free-viewpoint rendering for the closed scene composed of pre-captured objects," *ACM Transactions on Graphics (TOG)*, vol. 41, no. 4, pp. 101:1–101:10, 2022.
- [18] M. Tan, B. Chen, R. Pang, V. Vasudevan, M. Sandler, A. Howard, and Q. V. Le, "MnasNet: Platform-aware neural architecture search for mobile," in *IEEE Conference on Computer Vision and Pattern Recognition (CVPR)*, 2019.
- [19] T. Lin, P. Dollar, R. Girshick, K. He, B. Hariharan, and S. Belongie, "Feature pyramid networks for object detection," in *IEEE Conference on Computer Vision and Pattern Recognition (CVPR)*, 2017.
- [20] O. Ronneberger, P. Fischer, and T. Brox, "U-Net: Convolutional networks for biomedical image segmentation," in *Medical Image Computing and Computer-Assisted Intervention (MICCAI)*. Springer International Publishing, 2015, pp. 234–241.
- [21] D. Clevert, T. Unterthiner, and S. Hochreiter, "Fast and accurate deep network learning by exponential linear units (ELUs)," in *International Conference on Learning Representations (ICLR)*, 2016.
- [22] J. L. Ba, J. R. Kiros, and G. E. Hinton, "Layer normalization," 2016. [Online]. Available: <https://arxiv.org/abs/1607.06450>
- [23] M. Nagel, M. Fournarakis, R. A. Amjad, Y. Bondarenko, M. van Baalen, and T. Blankevoort, "A white paper on neural network quantization," 2021. [Online]. Available: <https://arxiv.org/abs/2106.08295>
- [24] J. Sturm, W. Burgard, and D. Cremers, "Evaluating egomotion and structure-from-motion approaches using the TUM RGB-D benchmark," in *IEEE/RIS International Conference on Intelligent Robot Systems (IROS)*, vol. 13, 2012.
- [25] S. Takamaeda-Yamazaki, "Pyverilog: A Python-based hardware design processing toolkit for Verilog HDL," in *Applied Reconfigurable Computing (ARC)*. Springer International Publishing, 2015, pp. 451–460.
- [26] "NNgen," 2017. [Online]. Available: <https://github.com/NNgen/nnngen>
- [27] J. Shotton, B. Glocker, C. Zach, S. Izadi, A. Criminisi, and A. Fitzgibbon, "Scene coordinate regression forests for camera relocalization in RGB-D images," in *IEEE Conference on Computer Vision and Pattern Recognition (CVPR)*, 2013.
- [28] A. Rahman, J. Lee, and K. Choi, "Efficient FPGA acceleration of convolutional neural networks using logical-3D compute array," in *Design, Automation and Test in Europe Conference and Exhibition (DATE)*, 2016, pp. 1393–1398.
- [29] T. Tsai, Y. Ho, and M. Sheu, "Implementation of FPGA-based accelerator for deep neural networks," in *IEEE International Symposium on Design and Diagnostics of Electronic Circuits and Systems (DDECS)*, 2019, pp. 1–4.
- [30] M. Rastegari, V. Ordonez, J. Redmon, and A. Farhadi, "XNOR-Net: ImageNet classification using binary convolutional neural networks," in *European Conference on Computer Vision (ECCV)*, 2016, pp. 525–542.
- [31] X. Zhang, J. Wang, C. Zhu, Y. Lin, J. Xiong, W. Hwu, and D. Chen, "DNNBuilder: an automated tool for building high-performance DNN hardware accelerators for FPGAs," in *IEEE/ACM International Conference on Computer-Aided Design (ICCAD)*, 2018, pp. 1–8.
- [32] X. Zhang, H. Ye, J. Wang, Y. Lin, J. Xiong, W. Hwu, and D. Chen, "DNNExplorer: A framework for modeling and exploring a novel paradigm of FPGA-based DNN accelerator," in *IEEE/ACM International Conference on Computer-Aided Design (ICCAD)*, 2020.
- [33] G. Lentaris, I. Stamoulias, D. Soudris, and M. Lourakis, "HW/SW codesign and FPGA acceleration of visual odometry algorithms for rover navigation on Mars," *IEEE Transactions on Circuits and Systems for Video Technology (TCSVT)*, vol. 26, no. 8, pp. 1563–1577, 2016.
- [34] J. Rettkowski, A. Boutros, and D. Göhlinger, "HW/SW co-design of the HOG algorithm on a Xilinx Zynq SoC," *Journal of Parallel and Distributed Computing*, vol. 109, pp. 50–62, 2017.
- [35] A. Hadj Fredj and J. Malek, "FPGA-accelerated anisotropic diffusion filter based on SW/HW-codesign for medical images," *Journal of Real-Time Image Processing (JRTIP)*, vol. 18, no. 6, pp. 2429–2440, 2021.
- [36] T. Van Chu, R. Kitajima, K. Kawamura, J. Yu, and M. Motomura, "A high-performance and flexible FPGA inference accelerator for decision forests based on prior feature space partitioning," in *International Conference on Field-Programmable Technology (ICFPT)*, 2021, pp. 1–10.
- [37] J. Gao, Y. Qian, Y. Hu, X. Fan, W. Luk, W. Cao, and L. Wang, "LETA: A lightweight exchangeable-track accelerator for efficientnet based on FPGA," in *International Conference on Field-Programmable Technology (ICFPT)*, 2021, pp. 1–9.